

Compensation of the laser parameters fluctuations in large ring laser gyros: a Kalman filter approach

Applied Optics

Alessandro Beghi¹, Jacopo Belfi^{2*}, Nicolò Beverini², B. Bouhade², D. Cuccato^{1,3},
Angela Di Virgilio⁴, and Antonello Ortolan³

¹*Department of Information Engineering, University of Padova Via Gradenigo 6/B,
Padova, Italy*

²*Department of Physics “Enrico Fermi,” Università di Pisa, and
CNISM unità di Pisa, Italy*

³*INFN National Laboratories of Legnaro, Viale dell’Università 2, Legnaro, Padova, Italy*

⁴*INFN Sez. di Pisa, Pisa, Italy*

**Corresponding author: belfi@df.unipi.it*

He-Ne ring laser gyroscopes are, at present, the most precise devices for absolute angular velocity measurements. Limitations to their performance come from the non-linear dynamics of the laser. Following the Lamb semi-classical theory, we find a set of critical parameters affecting the time stability of the system. We propose a method for estimating the long term drift of the laser parameters and for filtering out the laser dynamics effects from the rotation measurement. The parameter estimation procedure, based on the perturbative solutions of the laser dynamics, allow us to apply Kalman Filter theory for the estimation of the angular velocity. Results of a comprehensive Monte Carlo simulation and results of a preliminary analysis on experimental data from the ring laser prototype G-Pisa are shown and discussed. © 2012 Optical Society of America

1. Introduction

Ring laser “gyros” are standard sensors in estimating rotation rates relative to the inertial frame, with many applications ranging from inertial guidance [1], to angle metrology [2], geodesy [3,4], geophysics [5], as well to fundamental physics [5,6]. In the near future their

application is foreseen to improve the performances of advanced gravitational waves detectors [7] and also to provide ground based tests of General Relativity [8].

In a ring laser two oppositely traveling optical waves resonate inside a polygonal closed path. In an inertial frame, each beam follows a path of the same length. When the cavity rotates, a round-trip time difference between the co-rotating and counter-rotating beams occurs, as they experience a longer and a shorter path, respectively. This translates into a frequency difference of the two beams. Such frequency difference contains the information about the rotation rate of the reference frame.

This physical phenomenon is known as Sagnac effect and the Sagnac frequency ν_s (i.e. the frequency of the beat signal between the two beams), reads

$$\nu_s = \frac{4A}{\lambda L} \mathbf{n} \cdot \mathbf{\Omega}, \quad (1)$$

where A and L are the area and the perimeter of the cavity respectively, λ is the wavelength of the laser beam, \mathbf{n} is the normal vector of the plane of the ring cavity, $\mathbf{\Omega}$ is the rotation rate vector. In a real ring laser the laser dynamics are source of systematic errors in the estimate of ν_s . The laser dynamics are determined by a set of non linear equations that depend on parameters that are slowly varying, following random changes of the environmental conditions (mainly temperature and atmospheric pressure). In addition, the control of some parameters (e.g. laser emission frequency or light intensity) in a closed loop way may enhance the drifts of the others. Thus the simple Eq.(1) must be modified to take into account such complex behaviors (see for example [5]) which result in *i*) corrections to scale factor due to fluctuations of the laser gain, cavity losses and frequency detuning; *ii*) null shift due to any cavity non-reciprocity; and *iii*) non linear coupling between the two laser beams due to backscattering (at present, the most important instability source). Therefore, the beating signal can be represented as the sum of ν_s , white noise and terms arising from the non linear dynamics. Usually, the last ones are removed by long term correlations with a set of auxiliary sensors information, and by modeling the ring laser behavior with respect to the ideal case [9]. However, the non linearity of the dynamics limits the effectiveness of this approach. In this paper we propose to increase the ultimate resolution and the time stability of ring lasers by the estimation of the parameters of their system, and the subsequent application of an Extended Kalman filter (EKF) [10].

The proposed method has a very wide range of application. In fact, the parameter estimation and the dynamical filtering could improve the response of large size ring lasers, which have already reached accuracy of ~ 1 part in 10^9 , and so providing unique informations for geophysics and geodesy. Middle size rings, with sides of ~ 1 m, which are more affected by backscattering, will be improved as well. Such instruments are more suitable for geophysics applications (i.e. rotational seismology), and for application to gravitational waves

interferometers (e.g. local tilts measurements).

The paper is organized as follows. In Section 2 we discuss the non-linear dynamics of a He-Ne inhomogenously broadened ring laser. Here the critical parameters affecting ring behavior are presented. Section 3.B describes the implementation of the parameter estimation procedure and the Extended Kalman Filter (EKF) algorithm [10]. In Section 4 we presents the results of the parameter estimation procedure, and the performance of EKF for rotation estimation. The procedure has been tested on the experimental data of G-Pisa, and results are reported in Section 5. Finally, our conclusions are drawn in Section 6.

2. Dynamics of a Ring Laser

The differential equations of the ring laser dynamics were first derived long ago, using a low gain self consistent model by E. Lamb [11] for linear laser, and then extended to rings by F. Aronowitz [12]

$$\begin{aligned}\dot{I}_1 &= \frac{c}{L} \left[\alpha_1 I_1 - \beta_1 I_1^2 - \theta_{12} I_1 I_2 + 2r_2 \sqrt{I_1 I_2} \cos(\psi + \varepsilon) \right] \\ \dot{I}_2 &= \frac{c}{L} \left[\alpha_2 I_2 - \beta_2 I_2^2 - \theta_{21} I_1 I_2 + 2r_1 \sqrt{I_1 I_2} \cos(\psi - \varepsilon) \right] \\ \dot{\psi} &= \omega_s + \sigma_2 - \sigma_1 + \tau_{21} I_1 - \tau_{12} I_2 - \\ &\quad - \frac{c}{L} \left[r_1 \sqrt{\frac{I_1}{I_2}} \sin(\psi - \varepsilon) + r_2 \sqrt{\frac{I_2}{I_1}} \sin(\psi + \varepsilon) \right],\end{aligned}\tag{2}$$

where $I_{1,2}$, ψ and $\dot{\psi}$ are the dimensionless light intensities, the instantaneous phase difference, and the instantaneous circular beat frequency of the counter-propagating waves, respectively. Here $\omega_s = 2\pi\nu_s$ is the rotation rate in Eq.(1), and $\alpha_{1,2}, \sigma_{1,2}, \beta_{1,2}, \theta_{12,21}, \tau_{12,21}, r_{1,2}, \varepsilon$ are the Lamb parameters. It is worth mentioning that $\alpha_{1,2}, \sigma_{1,2}$ are the amplification minus losses, $\beta_{1,2}$ is the self saturation, $\theta_{12,21}, \tau_{12,21}$ describe cross-(mutual)-saturation, $r_{1,2}, \varepsilon$ are the amplitude and the relative phase of the backscattered waves, respectively. A more detailed explanation of the physical meaning of these parameters can be found in Appendix A.

2.A. Lamb parameters effects on the gyroscope performances

The study of Eqs.(2) has been conducted by several authors in the past [13–17], both with numerical and analytical approaches. The analytical solution cannot be found in the most general case, but only under certain approximations about the reciprocity of the system. Approximated analytical expressions for the time evolution of the Sagnac phase provide, nevertheless, an useful reference to better understand the role of the Lamb parameters noise on the estimation of the angular velocity ω_s .

We present in the following the periodic solution of Eqs.(2) in the case where: $I_1/I_2 = k$

and $\tau_{12} = \tau_{21} = 0$. In this case the phase equation takes the form:

$$\dot{\psi} = \omega_s - \frac{c}{L} \left[r_1 k \sin(\psi - \varepsilon) + \frac{r_2}{k} \sin(\psi + \varepsilon) \right] , \quad (3)$$

and admits the following solution:

$$\psi(t) = 2 \arctan \left[\frac{\Omega_{L1} + \Omega_p \tan \left(\frac{1}{2} \Omega_p t \right)}{\omega_s + \Omega_{L2}} \right] , \quad (4)$$

where $\Omega_{L1} = c/L(kr_1 + r_2/k) \cos(\varepsilon)$, $\Omega_{L2} = c/L(r_2/k - kr_1) \sin(\varepsilon)$ and $\Omega_p = \sqrt{\omega_s^2 - (\Omega_{L1}^2 + \Omega_{L2}^2)}$.

From Eq. (4), for $\Omega_{L1,L2} \ll \omega_s$, we get

$$\omega(t) \simeq \omega_s - \Omega_{L2} \cos \omega_s t - \Omega_{L1} \sin \omega_s t , \quad (5)$$

where ω denotes the detected Sagnac frequency and $\omega_{BS} \equiv -\Omega_{L2} \cos \omega_s t - \Omega_{L1} \sin \omega_s t$ represents the frequency modulation of the Sagnac signal.

In Figure 1 we report the results of a Monte Carlo simulation of 10^6 s of ring laser dynamics evolution with $I_1/I_2 = k$. We considered the following noise sources in the system: a white frequency noise with standard deviation of 10^{-1} on $\omega(t)$ (mimic of the output of AR(2) frequency detection algorithm [20]) and a random-walk noise on the parameters $r_{1,2}$, k , and ε . The Allan variance of $\omega(t)$ has been calculated for four different cases, denoted with (a), (b), (c) and (d).

In case (a) $(r_{1,2}, k, \varepsilon)$ are independent and vary in random walk with a step size of $(2 \cdot 10^{-9}, 10^{-3}, 10^{-2})$ respectively. In case (b) the only varying parameter is k , with a step size of 10^{-3} . In case (c) all parameters vary as in (a), but the processes r_1 and r_2 have been correlated with a correlation coefficient of 0.9 while ε varies around the nominal value of 0 rad with a random walk step size of 10^{-4} rad. In case (d) all parameters vary as in (b), but the process ε varies around the nominal value of $\pi/2$ rad with a random walk step size of 10^{-4} rad.

It can be easily observed that the noise contribution coming from the parameters fluctuation is transferred to the noise of the measured Sagnac frequency exhibiting the same random walk plus white noise pattern. The relative noise on the laser parameters is converted into frequency noise by the factor c/L meaning that the larger is the cavity perimeter, the larger is the rejection of the laser parameters noise. In addition, it is worth noticing that the backscattering phase ε plays a crucial role in transferring the fluctuations of r_1, r_2 on ω . It determines a strong reduction of the output noise for values close to $\varepsilon = \pi/2$ (trace (d)). In this regime, also known as 'conservative coupling regime' [14], the backscattered photons interact destructively and their influence on the nonlinear interaction between the two intracavity beams and the active medium is minimized.

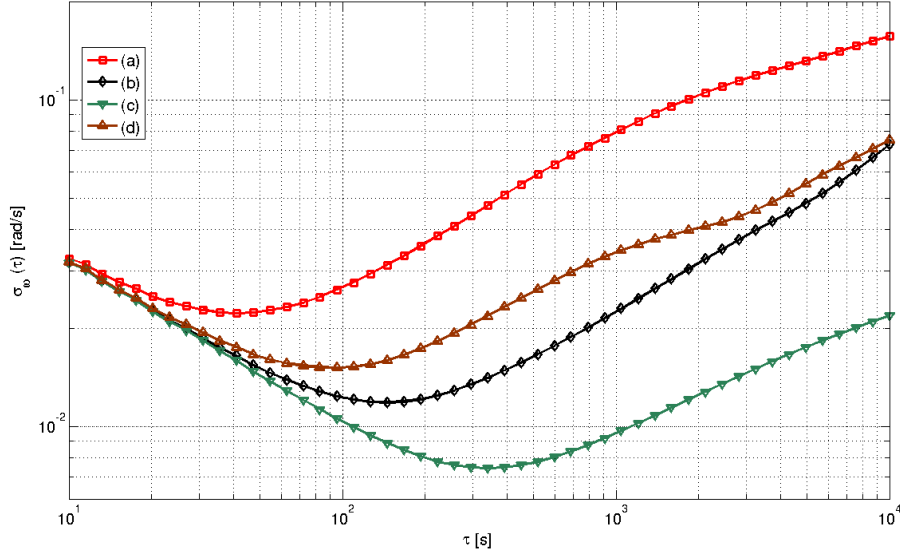


Fig. 1. Simulated Allan deviations of the estimated rotation rate. See the text for details.

In the next sections we will show that a statistical filtering procedure is able to identify the Lamb parameters, and to remove their slow drifts by using extended Kalman filtering. Thus the maximum resolution (i.e. the minimum value of $\sigma_\omega^2(\tau)$) and the time stability (i.e. the value of τ where the minimum is attained) of a ring laser can be significantly improved. In fact, the instantaneous Sagnac frequency will depend in general on the full system state $[I_1(t), I_2(t), \psi(t)]$, and so dynamic Kalman filtering can be more effective in estimating ω_s than other approaches that rely on $\psi(t)$ only (e. g. the standard $AR(2)$ method for frequency estimation [20]).

3. Dynamics of G-Pisa

G-Pisa is a prototype middle size He-Ne ring-laser. The main characteristics of its optical cavity are reported in table 1 while its experimental setup is sketched in figure 2.

The laser operation is controlled by two feedback loop systems, dedicated to the active stabilization of the optical frequency and the optical power [6]. The first loop keeps constant the frequency difference between the ring laser clockwise beam and a reference laser. It acts on two piezoelectric transducers ($PZT_{1,2}$) moving two opposite cavity mirrors along the cavity diagonal. The second loop regulates the RF discharge power in order to keep constant the power of the clockwise ring laser output.

G-Pisa dynamics can be derived from Eqs.(2) taking into account the spectroscopic prop-

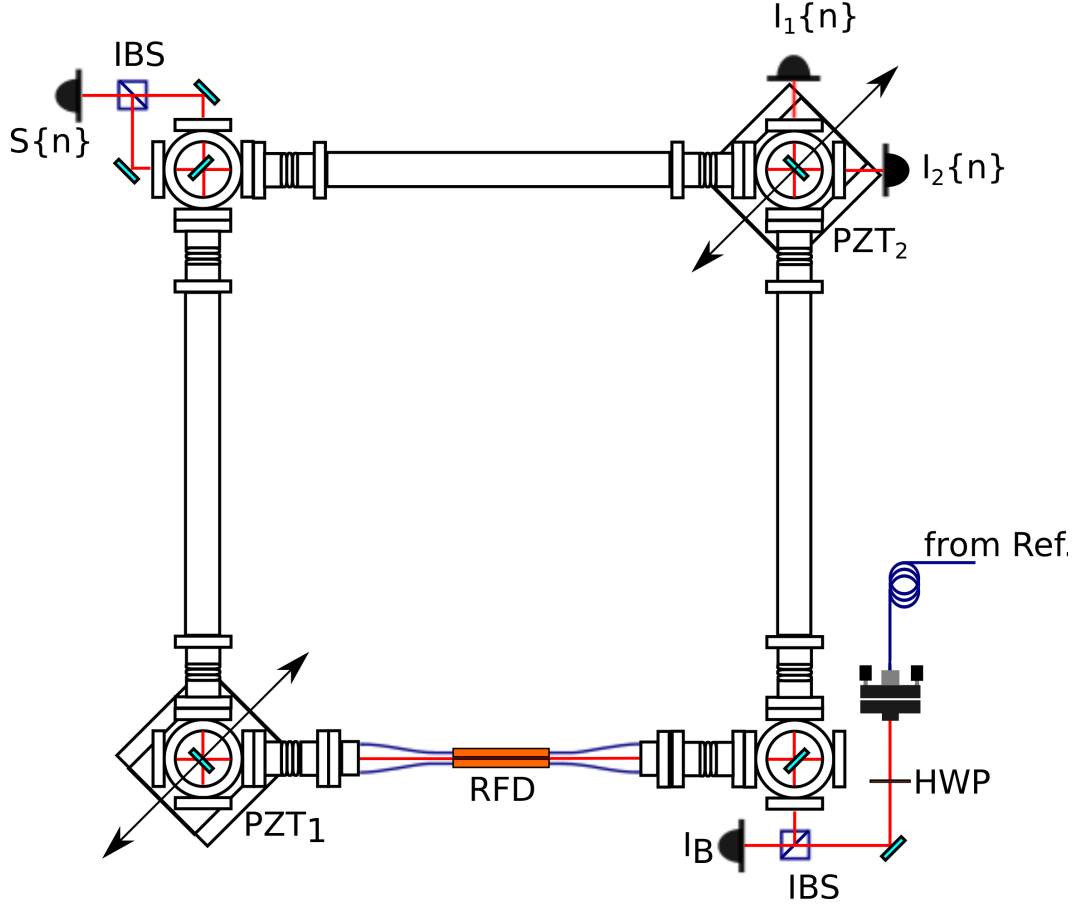


Fig. 2. G-Pisa experimental setup. The cavity vacuum chamber is entirely filled with a mixture of He-Ne and does not contain any intra-cavity element except for the four mirrors. $S_{\{n\}}$: Sagnac interference signal; $I_1\{n\}$: counter-clockwise single beam intensity; $I_2\{n\}$: clockwise single beam intensity; I_B : optical beat intensity; RFD: radio frequency discharge; IBS: intensity beam splitter; HWP: half wave-plate; PZT: piezoelectric transducer.

G-Pisa	
<i>Geometry</i>	
Cavity	square
Side length	1.35 m
Latitude	43° 40' 35.86"N
<i>Cavity mirrors</i>	
Radius of curvature	4 m
Total losses	3.7 ppm
Transmission	0.25 ppm
Scatter+absorption	3.5 ppm
<i>Optical properties</i>	
Wavelength	632.8 nm
Output power	1.6 nW (single mode)
Spatial mode	TEM ₀₀
Beam waist (s,h)	(1.97 mm, 2.43 mm)

Table 1. Main nominal characteristics of the “G-Pisa” apparatus. Mirrors characteristics are the nominal ones (manufacturer information) and refer to the single mirror for an incidence angle of 45°, and s-polarized light at 632.8 nm. Beam waists are reported as 4 times the 1/e² beam intensity radius.

erties of its active medium and the constraints imposed by the stabilization loops. The use of a special gas mixture, containing ²⁰Ne and ²²Ne isotopes at 50:50 ratio, avoids mode competition effects, while the perimeter control, by keeping constant the laser optical frequency avoids mode-jumps. In the Appendix A we show that $\beta_1 = \beta_2 = \beta$, $\sigma_1 = \sigma_2$, $\tau_{12} = \tau_{21} = 0$, and $\theta_{12} = \theta_{21} = 0$ hold for the closed loop operation of G-Pisa. Thus the equations of the dynamics reduced to:

$$\begin{aligned}
\dot{I}_1 &= \frac{c}{L} \left[\alpha_1 I_1 - \beta I_1^2 + 2r_2 \sqrt{I_1 I_2} \cos(\psi + \varepsilon) \right] \\
\dot{I}_2 &= \frac{c}{L} \left[\alpha_2 I_2 - \beta I_2^2 + 2r_1 \sqrt{I_1 I_2} \cos(\psi - \varepsilon) \right] \\
\dot{\psi} &= \omega_s - \frac{c}{L} \left[r_1 \sqrt{\frac{I_1}{I_2}} \sin(\psi - \varepsilon) + r_2 \sqrt{\frac{I_2}{I_1}} \sin(\psi + \varepsilon) \right] .
\end{aligned} \tag{6}$$

In Table 2 we report the typical Lamb parameters of G-Pisa, with a typical round-trip gain of $G = 3 \times 10^{-5}$. It is worth noticing that, as the perimeter is kept constant by moving the

ring mirrors, the backscattering phase angle ε is not fixed, but it ranges from 0 (conservative coupling) to $\pi/2$ (dissipative coupling) [14].

Parameter	Value	
ω_s	$2\pi \ 107.3 \text{ Hz} \simeq 674.5 \text{ rad/s}$	
α	4.3×10^{-9}	0.24 rad/s
β	1.5×10^{-5}	825 rad/s
r	2×10^{-7}	11.1 rad/s

Table 2. Typical values of Lamb parameters used in the simulations of G-Pisa dynamics with $G \sim 3 \cdot 10^{-5}$. In the first column the units are adimensional Lamb units. To compare the order of magnitude of effects with ω_s , in the second column we report such parameters multiplied by the free spectral range c/L .

3.A. Steady state approximated solutions

To provide suitable algorithms for parameter estimation, we study the steady state regime of Eqs.(6). By inspection of the right hand side of Eqs. (6), one finds that the general steady state solutions are periodic. In particular, without backscattering ($r_{1,2} = 0$), Eqs. (6) exhibit steady state solutions of the type

$$\begin{cases} I_1(t) &= \frac{\alpha_1}{\beta} \\ I_2(t) &= \frac{\alpha_2}{\beta} \\ \psi(t) &= \omega_s t \end{cases}, \quad (7)$$

for $t \rightarrow \infty$. In the presence of backscattering, the above solutions switch to periodic steady state solutions and exhibit oscillatory behaviors, and the backscattering can be treated as a perturbative sinusoidal forcing term. We can study the system oscillation around its unperturbed steady state by means of the time dependent perturbation theory [21]. To this aim we introduce the expansion parameter λ , which is assumed to be of the same order of magnitude of $r_{1,2}$ and write:

$$\begin{cases} \mathcal{I}_1(\lambda, t) &= \sum_{k=0}^{\infty} \frac{\lambda^k}{k!} I_1^{(k)}(t) \\ \mathcal{I}_2(\lambda, t) &= \sum_{k=0}^{\infty} \frac{\lambda^k}{k!} I_2^{(k)}(t) \\ \Psi(\lambda, t) &= \sum_{k=0}^{\infty} \frac{\lambda^k}{k!} \psi^{(k)}(t) \end{cases} \quad (8)$$

For $k = 0$, substituting the latter into the Eqs.(6), we recover the solution (7) with the positions $I_1^{(0)}(t) = \alpha_1/\beta$, $I_2^{(0)}(t) = \alpha_2/\beta$, $\psi^{(0)}(t) = \omega_s t$. The approximated solutions can be calculated iteratively from the series expansion in powers of λ of (8) into the dynamic of Eqs(6). A second order approximations of the solutions reads:

$$\left\{ \begin{array}{l} \mathcal{I}_1(t) \simeq \frac{\alpha_1}{\beta} + 2r_2\sqrt{\alpha_1\alpha_2} \frac{\alpha_1 \cos(\varepsilon + \omega_s t) + (\frac{\omega_s}{c/L}) \sin(\varepsilon + \omega_s t)}{\beta \left(\alpha_1^2 + (\frac{\omega_s}{c/L})^2 \right)} - 2 \frac{r_1 r_2 (c/L)}{\beta \omega_s} \sin(2\varepsilon) \\ \mathcal{I}_2(t) \simeq \frac{\alpha_2}{\beta} + 2r_1\sqrt{\alpha_1\alpha_2} \frac{\alpha_2 \cos(\varepsilon - \omega_s t) - (\frac{\omega_s}{c/L}) \sin(\varepsilon - \omega_s t)}{\beta \left(\alpha_1^2 + (\frac{\omega_s}{c/L})^2 \right)} + 2 \frac{r_1 r_2 (c/L)}{\beta \omega_s} \sin(2\varepsilon) \\ \Psi(t) \simeq (\omega_s - \frac{2r_1 r_2 (c/L)^2 \cos(2\varepsilon)}{\omega_s})t + (c/L) \frac{r_1 \sqrt{\frac{\alpha_1}{\alpha_2}} \cos(\varepsilon - \omega_s t) + r_2 \sqrt{\frac{\alpha_2}{\alpha_1}} \cos(\varepsilon + \omega_s t)}{\omega_s}, \end{array} \right. \quad (9)$$

where we made the additional approximation of keeping the leading terms in ω_s^n , with $n \leq 2$. Solutions (9) show a correction to the mean intensity level and pushing and pulling in the phase difference, as well as the presence of the first harmonic of ω_s .

3.B. Parameter Estimation and Kalman filtering

The Sagnac phase can be conveniently estimated by means of the Hilbert Transform (HT) of the interferogram $S(t) \simeq \sin \psi(t)$ which is routinely acquired during ring laser operation together with the monobeam intensities $I_1(t)$ and $I_2(t)$ [22]. Since ring laser signals are sampled, we shift to the discrete time domain, and from here on we denote time dependent intensities and Sagnac phase as $\{I_1(n)\}$, $\{I_2(n)\}$ and $\{\psi(n)\}$ ($n \in \mathbb{N}$), respectively.

Perturbative solutions and the least squares methods provide the main tools for estimation procedure of the parameters $\alpha_{1,2}$, $r_{1,2}$ and ε . For sake of clarity, we re-parametrize the measured intensities and Sagnac phase in the form

$$\left\{ \begin{array}{l} \mathcal{I}_1(t) = I_1 + i_1 \sin(\omega t + \phi_1) \\ \mathcal{I}_2(t) = I_2 + i_2 \sin(\omega t + \phi_2) \\ \Psi(t) = \omega t \end{array} \right. \quad (10)$$

as the quantities $I_{1,2}$, $i_{1,2}$ and $\phi_{1,2}$ can be readily estimated from $\{I_{1,2}(n)\}$ and $\{S(n)\}$. In fact, the mean intensities $I_{1,2}$ can be estimated by computing the sample average of $\{I_{1,2}(n)\}$. Moreover, the averaged modulation amplitudes $i_{1,2}$ and phase difference $\phi_1 - \phi_2$ at the fundamental frequency can be estimated by means of a digital lock-in procedure, which calculates the “in-phase” and “in-quadrature” components of $\{I_{1,2}(n)\}$. The reference

complex signal for the digital lock-in is given by the HT of $\{S(n)\}$. Averages are taken over a time interval where Lamb parameters remain fairly constant. The estimation procedure of Lamb parameters can be conveniently divided into two steps:

1. The first step is to estimate the phases of the intensities. From Eqs.(9) in the approximation $\frac{\omega_s}{(c/L)} \gg \alpha_{1,2}$ we have

$$\begin{cases} \phi_1 = \varepsilon \\ \phi_2 = -\varepsilon \end{cases} .$$

Thus we can immediately identify the backscattering angle from $\phi_{1,2}$ as

$$\widehat{\varepsilon} = \frac{\phi_1 - \phi_2}{2} , \quad (11)$$

where the hat symbol $\widehat{}$ denotes an identified parameter.

2. In the second step the remaining Lamb parameters are obtained by least squares methods. In fact, starting from the periodic steady state solutions (10), we can form the squared residuals

$$\begin{aligned} \Lambda(\alpha_1, \alpha_2, r_1, r_2) = & \frac{2\pi}{\omega} \times \\ & \times \int_0^{2\pi/\omega} \left\{ \dot{\mathcal{I}}_1 - \frac{c}{L} \left[\alpha_1 \mathcal{I}_1 - \beta \mathcal{I}_1^2 + 2r_2 \sqrt{\mathcal{I}_1 \mathcal{I}_2} \cos(\omega t + \widehat{\varepsilon}) \right] \right\}^2 + \\ & + \left\{ \dot{\mathcal{I}}_2 - \frac{c}{L} \left[\alpha_2 \mathcal{I}_2 - \beta \mathcal{I}_2^2 + 2r_1 \sqrt{\mathcal{I}_1 \mathcal{I}_2} \cos(\omega t - \widehat{\varepsilon}) \right] \right\}^2 dt \end{aligned} \quad (12)$$

averaged over a period $2\pi/\omega$. Minimization of $\Lambda(\alpha_{1,2}, r_{2,1})$ yields the best linear estimate of $\alpha_{1,2}$ and $r_{1,2}$; from the conditions $\partial\Lambda/\partial\alpha_1 = 0$, $\partial\Lambda/\partial\alpha_2 = 0$, $\partial\Lambda/\partial r_2 = 0$, and $\partial\Lambda/\partial r_1 = 0$, we get

$$\widehat{\alpha}_1 = \beta \left(I_1 + \frac{i_1^2}{4I_1} \right) + \frac{i_1 i_2 \omega}{4(c/L)I_2} \sin 2\widehat{\varepsilon} \quad (13)$$

$$\widehat{\alpha}_2 = \beta \left(I_2 + \frac{i_2^2}{4I_2} \right) - \frac{i_1 i_2 \omega}{4(c/L)I_1} \sin 2\widehat{\varepsilon} \quad (14)$$

$$\widehat{r}_1 = \frac{i_2 \omega}{2(c/L)\sqrt{I_1 I_2}} \quad (15)$$

$$\widehat{r}_2 = \frac{i_1 \omega}{2(c/L)\sqrt{I_1 I_2}} , \quad (16)$$

which fulfill the parameter estimation procedure via the second order approximation. It is worth noticing that one can increase the precision of the identified parameters by evaluating solutions of Eqs. (2) of higher order in λ and increase their accuracy by increasing the averaging time span.

4. Simulation results for G-Pisa

We briefly describe the specific implementation of the parameter estimation procedure for the G-Pisa ring laser, where the data are acquired at a sampling frequency of 5 kHz ($T_s = 200 \mu s$). To remove the oscillating component, intensity signals are low-pass filtered with a first order Butterworth filter with 1 Hz cutoff frequency. The quantities $I_{1,2}$ are estimated by averaging the decimated intensities over a time interval of 10 s (i.e. 5×10^4 samples). On the other side, to calculate the modulation $i_{1,2}$ and phases $\phi_{1,2}$, the intensities are first band-passed around the fundamental Sagnac band $[95 \div 125]$ Hz by means of a Butterworth filter, and decimated by a factor 2. The decimation procedure has been carried out by the tail recursive routine “Zoom and Decimation of a factor 2^n ” (ZD(n)), where each iteration step is composed by a half band filter stage with discrete transfer function $H(z) = \frac{z^3 + 2z^2 + 2z + 2}{4z^3 + 2z}$, followed by a downsampling by 2. The ZD(n) procedure ensures a linear phase filter response at least for $n = 3$ iterations, as no appreciable phase distortion was observed in simulated sinusoidal signals. The resulting data are then demodulated with a digital lock-in using as reference signal the discrete HT of the interferogram, and setting the integration time to 10 s. A schematic of the parameter estimation procedure is reported in Fig. 3. In addition, the phase of the two monobeam oscillating components is determined by the discrete HT, and their difference is estimated by unwrapping the phase angle and taking its average over 10 s. As a concluding remark on the parameter estimation procedure, we mention that the problem of filtering very long time series, has been solved by the “overlap and save” method [24], which is an efficient algorithm for avoiding the boundary transients due to finite length of digital filters.

Reliability of the parameter estimation routine is tested by Monte Carlo simulation of the dynamics of Eqs.(6) followed by the estimations of Lamb parameters from the simulated time series of $I_{1,2}$ and ψ . We run 10^4 simulations of the dynamics of Eqs.(6) allowing $\alpha_{1,2}$ and $r_{1,2}$ to vary according to normal distributions with mean as in Tab. 2 and standard deviation equal to 10% of their means. In addition, β is assumed constant, and ε uniformly distributed in $[0, \pi/2)$. In each simulation, we have compared the numerical RK4 solution of Eqs. (6) and approximated analytical solution (9) evaluated with the same Lamb parameters. We found that they are in a very good agreement, with means of the relative errors on $I_1(t)$, $I_2(t)$ and $\psi(t)$ of -6.4×10^{-7} , -6.2×10^{-7} and -1.5×10^{-5} , and standard deviations of 4.6×10^{-6} , 4.6×10^{-6} and 1.3×10^{-6} , respectively.

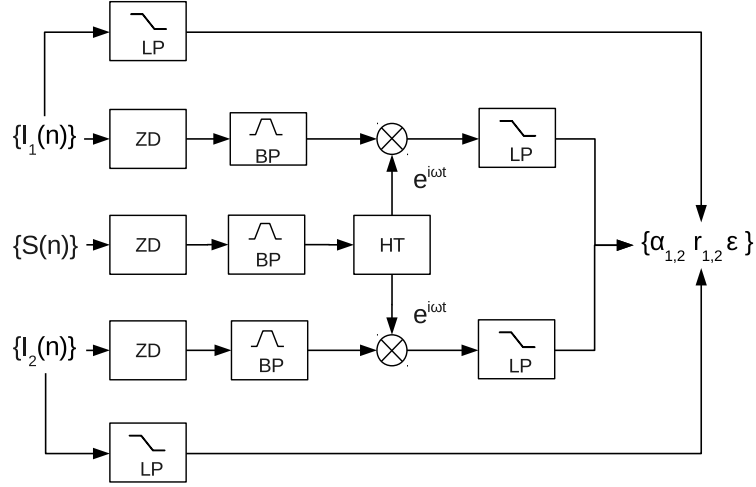


Fig. 3. Schematic of the parameter estimation procedure, where LP \rightarrow low-pass Butterworth filter, BP \rightarrow bandpass Butterworth filter, ZD \rightarrow Zoom and Decimation routine, HT \rightarrow Hilbert transform (see text).

To numerically assess the performance of the parameter estimation procedure, we run a simulation of 6 hours where $\alpha_{1,2}$, $r_{1,2}$, ϵ and ω_s fluctuate following independent random walk processes with self-correlation time of 1 hour. To reproduce the experimental behavior of a ring laser, the time drift of ω_s , which mimics the effects of local tilts and rotations, is a factor of 5 lower than the auto-correlation time of the other parameters. We superimposed to the simulated data an additive white noise, with $\text{SNR} = 10^2$ for the beam intensities and $\text{SNR} = 5 \times 10^3$ for the interferogram. Such order of magnitudes are routinely achieved in large ring laser [25] and in G-Pisa [6]. The results we got are summarized in Fig. 4, Fig. 5 and Fig. 6.

The overall accuracy of the Lamb parameter estimation procedure is good, with a relative standard deviation of 3×10^{-3} and 4×10^{-3} in the estimation of $\alpha_{1,2}$, and $r_{1,2}$, respectively. The absolute error in the estimation of the backscattering phase is 3×10^{-3} rad. The attained accuracy is not far from the lower bound $\sim 10^{-4}$ associated to the level of the observation noise of $\{I_1(n)\}$, $\{I_2(n)\}$ and $\{\psi(n)\}$.

4.A. Estimation of ω_s by Kalman filtering

Knowledge of the Lamb parameters $\hat{\alpha}_{1,2}$, $\hat{r}_{1,2}$ and $\hat{\epsilon}$, together with the β parameter separately acquired, allow us to set up an Extended Kalman Filter [10] for the estimation of the rotation

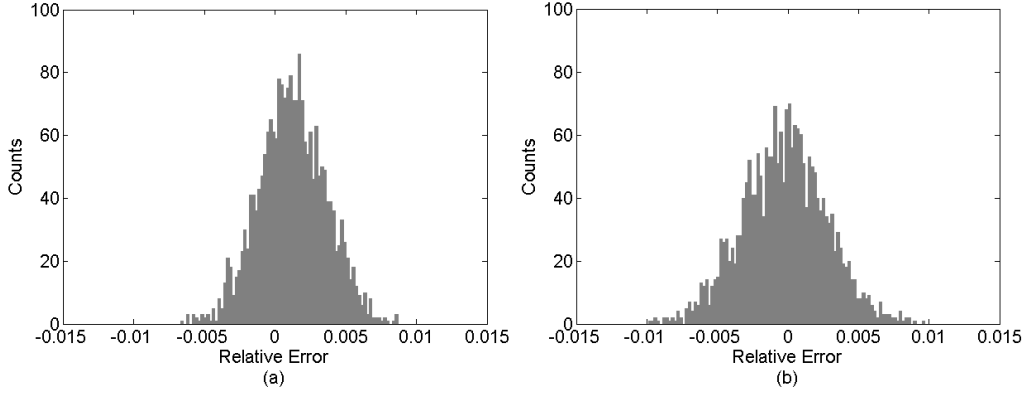


Fig. 4. Histograms of the relative errors $(\hat{\alpha}_{1,2} - \alpha_{1,2})/\alpha_{1,2}$ that affect the estimation of Gain minus losses parameters calculated with 2×10^4 realizations of the ring laser dynamics. (a) Histogram relative to α_1 : mean 1.4×10^{-3} and standard deviation 2.9×10^{-3} ; (b) histogram relative to α_2 : mean -2.5×10^{-4} and standard deviation 3.9×10^{-3} .

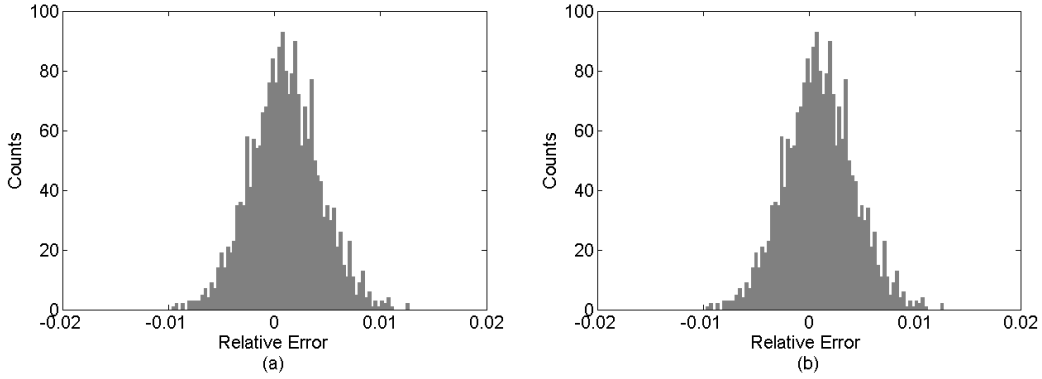


Fig. 5. Histograms of the relative errors $(\hat{r}_{1,2} - r_{1,2})/r_{1,2}$ that affect the estimation of backscattering coefficients calculated with 2×10^4 realizations of the ring laser dynamics. (a) Histogram relative to r_1 : mean 1.1×10^{-3} and standard deviation 4.6×10^{-3} ; (b) histogram relative to r_2 : mean 1.3×10^{-3} and standard deviation 3.2×10^{-3} .

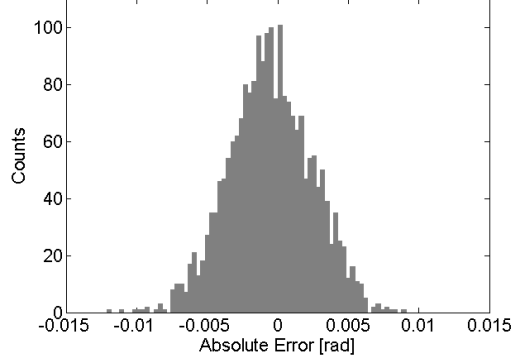


Fig. 6. Histogram of the absolute errors $\hat{\varepsilon} - \varepsilon$ that affect the estimation of backscattering phase calculated with 2×10^4 realizations of the ring laser dynamics; mean -4.3×10^{-4} rad and standard deviation 2.8×10^{-3} rad.

rate $\hat{\omega}_s$.

The EKF state variables are the \mathbb{R}^3 vector $\mathbf{X}(t) \equiv [I_1(t), I_2(t), \psi(t)]^T$. The dynamics model is given by Eqs.(6), with the addition of the model error as a zero mean, white, stochastic vector field $\mathbf{v}(t)$ with variance $\text{Var}[\mathbf{v}(t)] \equiv Q$, where Q is a 3×3 covariance matrix that accounts for the effects of unmodeled dynamics, for instance, identified parameter errors, calibration errors, and numerical integration inaccuracies. The EKF prediction step, which corresponds to the integration of Eqs.(6) over the time interval T_s , is carried out using the RK4 Runge-Kutta routine.

In the discrete time domain, the model of the measurement process reads $\{\mathbf{y}(n)\} = \{\mathbf{X}(n)\} + \{\mathbf{w}(n)\}$, where $\mathbf{w}(n)$ is zero mean, white, stochastic vector field (observation noise) with variance $\text{Var}[\mathbf{w}(n)] \equiv R$, and R is a 3×3 covariance matrix. In the standard experimental set up of ring lasers $[I_1(t), I_2(t), \psi(t)]$ are measured by independent sensors, and so we can assume that R is diagonal, with diagonal elements the observation noise variances $\sigma_{I_1}^2, \sigma_{I_2}^2, \sigma_\psi^2$ which can be conveniently calculated through the level of white noise in the power spectrum of $\{\mathbf{y}(n)\}$.

The backscattering frequency is estimated from the filtered channels $\hat{I}_{1,2}(n)$, $\hat{\psi}(n)$, the identified parameters $\hat{\alpha}_{1,2}$, $\hat{r}_{1,2}$, $\hat{\varepsilon}$, and the exogenous parameter β as

$$\hat{\omega}_{BS} = \frac{c}{L} \left[\hat{r}_1 \sqrt{\frac{\hat{I}_1}{\hat{I}_2}} \sin(\hat{\psi} - \hat{\varepsilon}) + \hat{r}_2 \sqrt{\frac{\hat{I}_2}{\hat{I}_1}} \sin(\hat{\psi} + \hat{\varepsilon}) \right]$$

where, for simplicity, we have dropped the index (n) from time series. The Sagnac frequency is then estimated from the difference $\hat{\omega}_s = \dot{\hat{\psi}} - \hat{\omega}_{BS}$, where the numerical derivative of $\hat{\psi}$ has

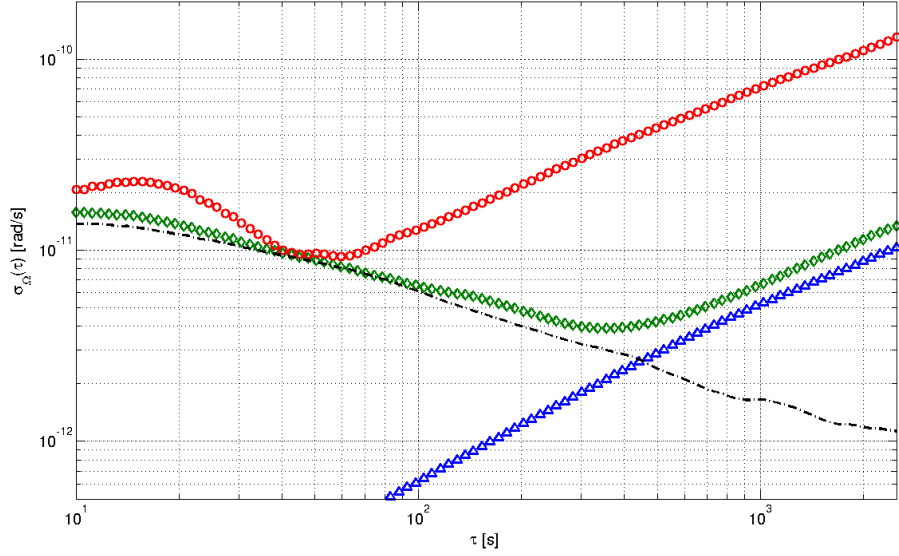


Fig. 7. Allan standard deviation of the rotation rate estimated by AR(2) method (circles) and Extended Kalman Filter (open diamonds) using 2×10^4 seconds of the Monte Carlo simulation with random walk of Lamb Parameters. For comparison, we also plot the Allan standard deviation of the simulated rotational drift (open triangles), and the Allan standard deviation of the EKF estimation after the subtraction of the rotational drift (dash dotted line).

been computed by the “5 point method” [18] designed to reject the derivative amplification of the noise.

The capability of the EKF in increasing the time stability and the resolution of the gyroscope has been tested with a 6 hours simulation of the ring laser dynamics with parameter variations as in the parameter estimation tests. The results are summarized in Fig.7 where we compared the Allan variance of AR(2) and EKF frequency estimations. We conclude that, for this simulation with typical parameters of middle-size rings, the rotational resolution increases by a factor of 10 while the minimum of the Allan standard deviation shifts from 60 s to 360 s.

5. Application to real data

To run the parameter estimation routine on the G-Pisa data, the photodetector signals $V_{1,2}(t)$ have been converted to dimensionless intensities $I_{1,2}(t)$ (Lamb units), using the following

relation

$$I_{1,2}(t) = c_{Lamb} \frac{V_{1,2}(t)}{G_{ph} a_{eff}} \equiv c_{Lamb} P_{out\,1,2}, \quad (17)$$

where: $G_{ph} = 10^9$ V/A is the photo-amplifiers gain, $a_{eff} = 0.4$ A/W is the quantum efficiency of the photo-diodes, and $c_{Lamb} = 3.5 \times 10^6$ W⁻¹ is the calibration constant to Lamb units (see Appendix A); $P_{out\,1,2}$ is the output power in Watt. The parameter estimation for G-Pisa is completed by the acquisition and calibration of the β parameter.

In Fig. 8 we show the comparison between the real time series measured on the G-Pisa ring laser and the calculated signal by the model after the parameter estimation according to the scheme in Fig. 3.

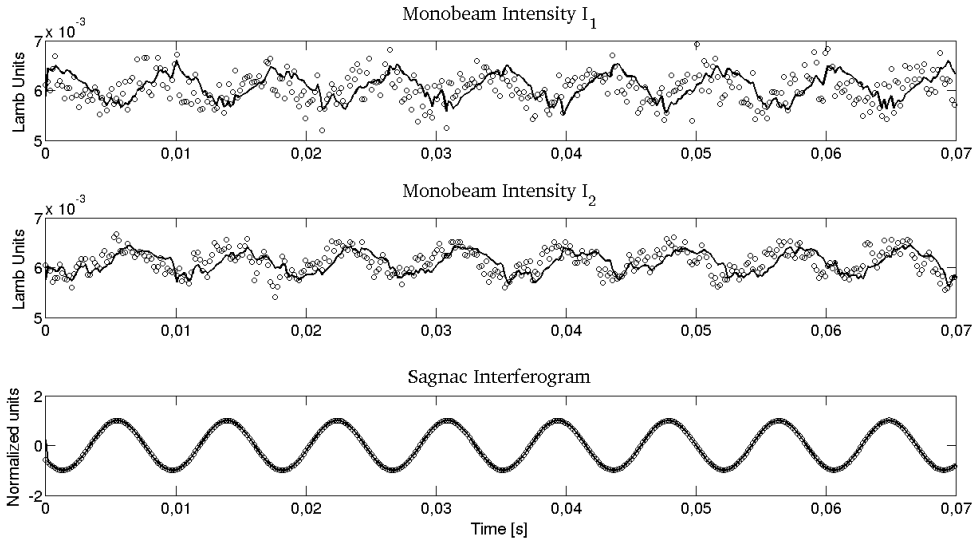


Fig. 8. Extended Kalman Filter estimation of $I_1(n)$, $I_2(n)$ and $\sin \psi(n)$. Circles: G-Pisa raw data sampled at 5 kHz. Continuous line: filter output.

In Fig. 9 we show the time series of the identified parameters for the G-Pisa ring laser and the calibrated parameter β , using the routine described in Section 3.B.

After the estimation of the G-Pisa parameters, we apply the EKF to the light intensities and to the interferogram (see [22]). However, the implementation of the EKF requires an estimation of the covariance matrices Q and R of observation and model errors. Typically Q and R are considered as tuning parameters and set on the base of trial-and-error procedures. In fact, we started from an initial raw estimation for the diagonal elements of Q and R using simulations and power spectra of $I_{1,2}$ and ψ , respectively. Then we tuned these values searching for the minimum of the Allan variance of ω_s and came to $Q = \text{diag}(10^{-8}, 10^{-8}, 10^{-10})$ and

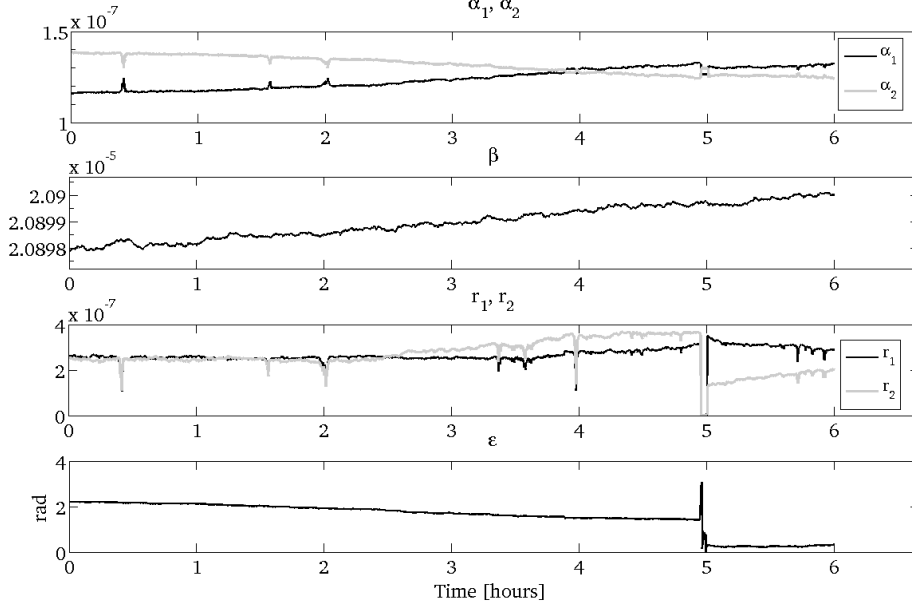


Fig. 9. Time series of $\alpha_{1,2}$, $r_{1,2}$ and ε and of β , respectively estimated and calibrated using 6 hours of experimental data of G-Pisa.

$R = \text{diag}(10^{-8}, 10^{-8}, 10^{-8})$. The performance of parameter estimation and EKF were limited by the environmental conditions of G-Pisa, e.g. local tilts and spurious rotations induced by the granite slab that support the instrument and some electronic disturbances, as it can be seen in Fig. 10, where we report the power spectrum of $\{S(n)\}$.

In figure 11 we report the Allan standard deviation of the Sagnac frequency estimated with AR(2) and EKF. An increase of a factor of 1.5 in rotation-rate resolution and of a factor of 2 in the time stability is observed.

6. Conclusions

A full model of the ring laser dynamics has been studied and applied to the estimation and removal of the long term drift in the laser parameters. The proposed data processing technique is based on the estimation of the parameters appearing in the Lamb equations for a He-($^{20}\text{Ne} + ^{22}\text{Ne}$) ring laser. Results of Monte Carlo simulations supported the viability of the parameter estimation, and yielded a relative estimation error of the order of 3×10^{-3} for $\alpha_{1,2}$ and $r_{1,2}$ and an estimation error $\sim 10^{-3}$ rad for ε . The accurate estimation of the Lamb parameters allows for the application of the Kalman Filter for the estimation of the rotation rate from the Sagnac frequency. Simulations showed a significant improvement in the frequency estimation by EKF compared to AR(2) method. Preliminary results on data from the ring laser prototype G-Pisa, presently strongly affected by local rotational noise,

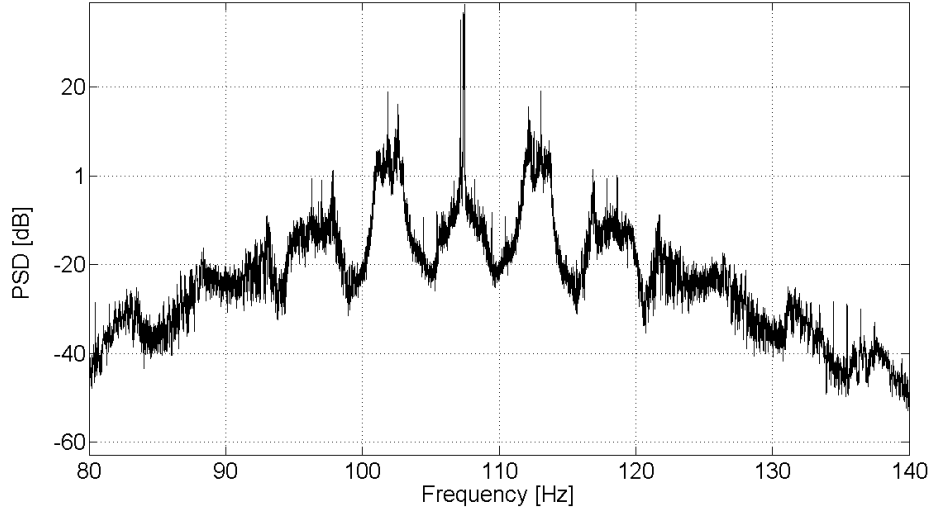


Fig. 10. Power spectrum of the interferogram data around the Sagnac frequency ~ 107.3 Hz.

make us confident about the reliability of our approach in the presence of unmodeled experimental noise and calibration errors. Our approach can be further improved, and different mathematical tools can be used. For instance, the numerical integration method RK-4 can be substituted by geometrical integrators, or modified in conservative routines [27]. EKF can be also improved by increasing the state dimension, modifying the observation model and the estimation of ω_s . As a final remark, we note that ring lasers achieved world record in rotation sensitivity, accuracy and time stability with sophisticated hardware, accurate selection of the working point of the He-Ne laser, despite a very basic off-line analysis. In this paper, we have shown that the parameters of the ring laser dynamics can be identified and their effects on resolution and time stability removed notwithstanding the system non linearities. We think that data analysis will cooperate more and more with ring laser hardware in pushing the resolution and the time stability of ring lasers beyond the current limitations.

References

1. N. Barbour and G. Schmidt, “Inertial Sensor Technology Trends,” *Sensors Journal*, IEEE, **1**, 4, 332 - 339 (2001).
2. Yu. V. Filatov, D. P. Loukianov and R. Probst, “Angle measurement by laser goniometer,” *Metrologia* **34**, 343 (1997).
3. K. U. Schreiber, A. Velikoseltsev, M. Rothacher, T. Klügel, G.E. Stedman and D.L. Wiltshire, “Direct measurement of diurnal polar motion by ring laser gyroscopes,” *J.*

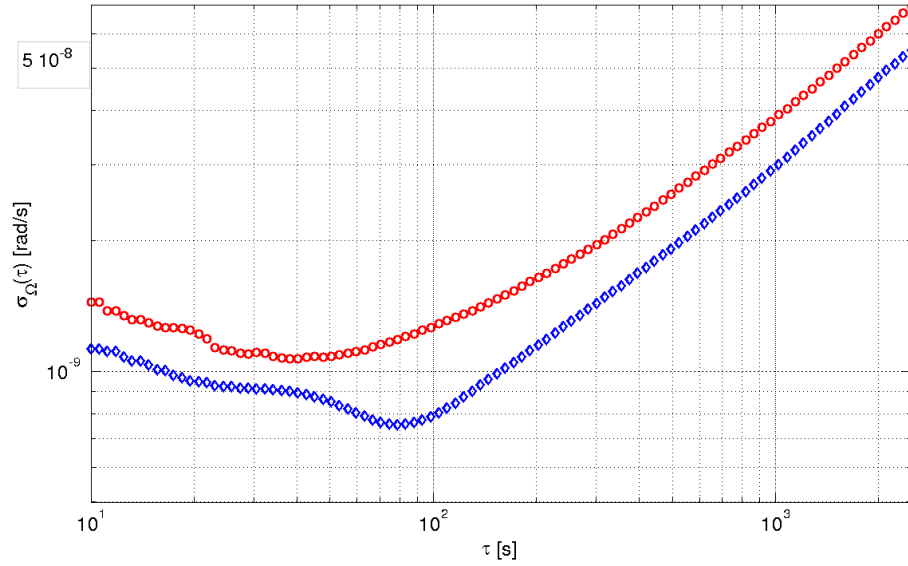


Fig. 11. Allan standard deviation of the rotation rate estimated by AR(2) method (circles) and Extended Kalman Filter (open diamonds) using 2×10^4 seconds of experimental data of G-Pisa.

- Geophys. Res. **109**, B06405 (2004);
4. K. U. Schreiber, T. Klügel, J.-P. R. Wells, R. B. Hurst, and A. Gebauer, “How to detect the Chandler and the annual wobble of the earth with a large ring laser gyroscope,” *Phys. Rev. Lett.* **107**, 173904 (2011).
 5. G. E. Stedman, *Rep. Prog. Phys.*, “Ring-laser tests of fundamental physics and geophysics,” **60**, 615-688 (1997).
 6. J. Belfi, et al., “A 1.82 m² ring laser gyroscope for nano-rotational motion sensing,” *Applied Physics B* **106**, 2, 271-281 (2011).
 7. A. Di Virgilio et al., “Performances of ‘G-Pisa’: a middle size gyrolaser,” *Class. Quantum Grav.* **27**, 084033 (2010).
 8. F. Bosi et al., “Measuring Gravito-magnetic Effects by Multi Ring-Laser Gyroscope,” *Phys. Rev. D*, **84**, 122002 (2011).
 9. See e.g. A. Velikoseltsev, *The development of a sensor model for Large Ring Lasers and their application in seismic studies* Ph.D. Thesis, Technische Universität München, Germany (2005) and references therein.
 10. A.H. Jazmiski, *Stochastic Processes and Filtering Theory* (Academic Press New York 1970).

11. L. N. Menegozzi and W. E. Lamb, "Theory of a ring laser," *Phys. Rev. A* **8**, 4 (1973).
12. F. Aronowitz, "Fundamentals of Ring Laser Gyro," in *Optical Gyros and their Applications*, RTO AGARDograph 339, 23-30, (1999).
13. F. Aronowitz and R. J. Collins, "Lock-In and Intensity-Phase Interaction in the Ring Laser," *Journal of Applied Physics*, **41**, 1 (1970).
14. G. E. Stedman, Z. Li, C. H. Rowe, A. D. McGregor and H. R. Bilger, "Harmonic analysis in a precision ring laser with back-scatter induced pulling," *Phys. Rev. A*, **51**, 6 (1995).
15. R. Christian and L. Mandel, "Frequency dependence of a ring laser with backscattering," *Phys. Rev. A*, **34**, 5 (1986).
16. L. Pesquera, R. Blanco, and M. A. Rodriguez, "Statistical properties of gas ring lasers with backscattering," *Phys. Rev. A*, **39**, 11 (1989).
17. C. Etrich, Paul Mandel, R. Centeno Neelen, R. J. C. Spreeuw, and J. P. Woerdman, "Dynamics of a ring-laser gyroscope with backscattering," *Phys. Rev. A*, **46**, 11 (1992).
18. W. H. Press, S. A. Teukolsky, W. T. Vetterling, and B. P. Flannery, *Numerical Recipes 3rd Edition, The Art of Scientific Computing* (Cambridge University Press, Cambridge, Sept. 2007).
19. A. Papoulis, *Probability, Random Variables, and Stochastic Processes* (McGraw-Hill, New York 1984).
20. D.P. McLeod, B.T. King, G.E. Stedman, T.H. Webb, and K.U. Schreiber, "Autoregressive analysis for the detection of earthquakes with a ring laser gyroscope," *Fluctuation and Noise Letters*, **1**, 1, R41-R50 (2001).
21. H. Goldstein, *Classical Mechanics* (Addison-Wesley 1980 London) ISBN10, 020102918-9.
22. By definition, the interferogram of the two counter-propagating beams is given by $S(t) = I_1(t) + I_2(t) - 2\sqrt{I_1(t)I_2(t)}\sin(\psi(t))$. However, to estimate $\sin(\psi(t))$ directly from $S(t)$, the linear trend $I_1(t) + I_2(t)$ is removed, and the energy $I_1(t)I_2(t)$ is normalized to 1 over time intervals which usually correspond to thousands of cycles.
23. H. Cramér, *Mathematical Methods of Statistics* (Princeton Univ. Press. 1946 Princeton NJ) ISBN 0-691-08004-6.
24. J. G. Proakis and D. G. Manolakis, *Digital Signal Processing* (Macmillan Pub. Comp. 1992 New York) ISBN-10: 002396815X.
25. K. U. Schreiber, T. Klügel, A. Velikoseltsev, W. Schlüter, G. E. Stedman, J. -P. R. Wells, "The Large Ring Laser G for Continuous Earth Rotation Monitoring," *Pure and Applied Geophysics*, **166**, 8-9 (2009).
26. P. W. Smith, "Linewidth and Saturation Parameters for the 6328 Å Transition in a He-Ne Laser," *Journal of Applied Physics*, **37**, 2089-2093 (1965).
27. E. Hairer, C. Lubich and G. Wanner, *Geometric Numerical Integration* (Springer 2006 Berlin).

A. Lamb Coefficients calculation

The two intensities I_1 and I_2 in Eqs.(2) are expressed in Lamb Units

$$I_{1,2} = \frac{|\mu_{ab}|^2(\gamma_a + \gamma_b)}{4\hbar^2\gamma_a\gamma_b\gamma_{ab}} E_{1,2}^2 = \frac{|\mu_{ab}|^2(\gamma_a + \gamma_b)}{4\hbar^2\gamma_a\gamma_b\gamma_{ab}} \cdot \frac{P_{out1,2}}{2c\epsilon_0 s_b T} \equiv c_{Lamb} P_{out1,2}$$

where

$$\mu_{ab} = \sqrt{\pi\epsilon_0 \frac{\lambda^3}{(2\pi)^3} \hbar A_{ik}} ,$$

is the electric-dipole matrix element between the laser states $a = 3s^2$ and $b = 2p^4$ (i.e. the upper and the lower of the laser energy levels), γ_a and γ_b are the decay rates in Paschen notation, $\eta = \gamma_{ab}/\Gamma_D$ is the ratio between the homogeneous and the Doppler broadening of the laser transition. Here $\Gamma_D = \sqrt{2k_b T_p / m_{ne}} / \lambda$, where k_b is the Boltzmann constant, m_{ne} is the atomic mass of Neon and T_p is the plasma temperature. A_{ik} is the radiative decay rate between the laser levels, $E_{1,2}$ are the electric fields amplitudes, $P_{out1,2}$ are the output powers, ϵ_0 is the dielectric constant of vacuum, s_b is the area of the transverse section of the beam, T is the transmission coefficient of the mirror, and \hbar is the reduced Plank constant. The table 3 contains the reference values of the above quantities for a Doppler broadened active medium in presence of collision, according to refs. [11] and [26].

s_b	$18 \cdot 10^{-6} \text{ m}^2$
P_{out}	$1 - 10 \text{ nW}$
p	5.25 mbar
γ_a	12 MHz
γ_b	127 MHz
γ_{ab}	234 MHz
T_p	450 K
μ_{ab}	$3.2 \cdot 10^{-30} \text{ C m}$

Table 3. The G-Pisa laser parameters.

The coefficients in Eq.(2) can be calculated by means of the plasma dispersion function, which is the function associated to the broadening profile of the laser transition

$$Z(\xi_{1,2}) = 2i \int_0^\infty e^{-x^2 - 2\eta x - 2i\xi_{1,2}x} dx , \quad (18)$$

where $\xi_{1,2} = (\omega_{1,2} - \omega_0)/\Gamma_D$ is the detuning, normalized to the Doppler width, from the transition center for the beams 1 and 2. The independent variables $\xi_{1,2}$ are in correlation with

temperature and pressure inside the cavity. For an active medium composed by a gas mixture of two isotopes, one has to account for ξ and ξ' , η and η' , Γ_D and Γ'_D . Here the unprimed and primed symbols refer to the Ne isotopes 20 and 22, respectively. In the Doppler limit $\eta \ll 1$ and $\eta' \ll 1$, which is common for middle or large size He-Ne rings, $Z(\xi)$ is usually approximated as

$$\begin{aligned} Z_I(\xi) &\simeq \sqrt{\pi} e^{-\xi^2} - 2\eta \\ Z_R(\xi) &\simeq -2\xi e^{-\xi^2} \end{aligned} ,$$

where the pedices I and R stands for imaginary and real part, respectively. Within the above approximations the Lamb coefficients have the following expressions

$$\begin{aligned} \alpha_{1,2} &= \frac{G}{Z_I(0)} [k Z_I(\xi_{1,2}) + k' Z_I(\xi'_{1,2})] - \mu_{1,2} \\ \beta_{1,2} &= \alpha_{1,2} + \mu_{1,2} \\ \sigma_{1,2} &= \frac{f_0}{2} \frac{G}{Z_I(0)} [k Z_R(\xi_{1,2}) + k' Z_R(\xi'_{1,2})] \\ \theta_{12} &= \frac{\Gamma G}{Z_I(0)} \left[k \frac{Z_I(\xi_{1,2})}{1 + (\xi_m/\eta)^2} + k' \frac{Z_I(\xi'_{1,2})}{1 + (\xi'_m/\eta)^2} \right] \\ \tau_{12} &= \frac{\Gamma f_0}{2} \frac{G}{Z_I(0)} \left[k \frac{Z_I(\xi_{1,2}) \xi_m/\eta}{1 + (\xi_m/\eta)^2} + k' \frac{Z_I(\xi'_{1,2}) \xi'_m/\eta}{1 + (\xi'_m/\eta)^2} \right] , \end{aligned} \tag{19}$$

where G is the laser gain, $\Gamma = (\gamma_a + \gamma_b)/(2\gamma_{ab})$, $\xi_m = (\xi_1 + \xi_2)/2$, $\xi'_m = (\xi'_1 + \xi'_2)/2$, $\mu_{1,2}$ are the mirror losses experienced by each beam, k and k' are the fractional amount of isotopes in the gas mixture. The equation for θ_{21} and τ_{21} are obtained from the expression of θ_{12} and τ_{12} by permuting the subscripts 1 and 2. Substituting $\xi_{1,2} \simeq 0.47$, $\xi'_{1,2} \simeq -0.49$, $k = k' = 0.5$, $G \simeq 3 \times 10^{-5}$, $\eta \simeq 0.25$, and $\mu_{1,2} \simeq 1, 48 \times 10^{-5}$ in Eqs. (19) we get for the closed loop operation of G-Pisa $\beta_1 - \beta_2 \simeq 10^{-14}$, $\theta_{12,21} \simeq 8 \times 10^{-8}$, $\tau_{12,21} \simeq 10^{-1}$, and the values in Table 2.